Biophysical Journal
Article

Biophysical Society

Predicted Effects of Severing Enzymes on the Length Distribution and Total Mass of Microtubules

Yin-Wei Kuo,[1,2] Olivier Trottier,[2,3] and Jonathon Howard[2,*]
[1]Department of Chemistry, [2]Department of Molecular Biophysics and Biochemistry, and [3]Department of Physics, Yale University, New Haven, Connecticut

ABSTRACT Microtubules are dynamic cytoskeletal polymers whose growth and shrinkage are highly regulated as eukaryotic cells change shape, move, and divide. One family of microtubule regulators includes the ATP-hydrolyzing enzymes spastin, katanin, and fidgetin, which sever microtubule polymers into shorter fragments. Paradoxically, severases can increase microtubule number and mass in cells. Recent work with purified spastin and katanin accounts for this phenotype by showing that, in addition to severing, these enzymes modulate microtubule dynamics by accelerating the conversion of microtubules from their shrinking to their growing states and thereby promoting their regrowth. This leads to the observed exponential increase in microtubule mass. Spastin also influences the steady-state distribution of microtubule lengths, changing it from an exponential, as predicted by models of microtubule dynamic instability, to a peaked distribution. This effect of severing and regrowth by spastin on the microtubule length distribution has not been explained theoretically. To solve this problem, we formulated and solved a master equation for the time evolution of microtubule lengths in the presence of severing and microtubule dynamic instability. We then obtained numerical solutions to the steady-state length distribution and showed that the rate of severing and the speed of microtubule growth are the dominant parameters determining the steady-state length distribution. Furthermore, we found that the amplification rate is predicted to increase with severing, which is, to our knowledge, a new result. Our results establish a theoretical basis for how severing and dynamics together can serve to nucleate new microtubules, constituting a versatile mechanism to regulate microtubule length and mass.

SIGNIFICANCE The numbers and lengths of microtubules are tightly regulated in cells. Severing enzymes fragment microtubules into shorter filaments and are important for cell division and tissue development. Previous work has shown that severing can lead to an increase in total microtubule number and mass, but the effect of severing on microtubule length is not understood quantitatively. Combining mathematical modeling and computational simulation, we solve the microtubule length distribution in the presence of severing enzymes and explore how severing activity and microtubule dynamics collectively control microtubule number and length. These results advance our understanding of the physical basis of severing as a regulatory mechanism shaping the cellular cytoskeletal network.

INTRODUCTION

The cytoskeleton is a network of filamentous polymers and is found in all living organisms, including bacteria, plants, and animals. Microtubules form one component of the eukaryotic cytoskeleton. They elongate from their ends by addition of tubulin subunits and alternate between phases of slow growth and rapid shrinkage. This alternation, termed dynamic instability, causes frequent turnover of polymer and exchange of tubulin subunits with the soluble pool (1,2). The dynamics of microtubules can be described quantitatively by four parameters: the growth (polymerization) rate, the shrinkage (depolymerization) rate, the catastrophe frequency (the transition from the growing to the shrinking state), and the rescue frequency (the transition from the shrinking to the growing state) (2,3). As eukaryotic cells undergo cell division, migration, or shape change, microtubule-associated proteins (MAPs) regulate the dynamics of microtubules so as to alter their numbers and lengths (4). Much is known about the mechanisms by which MAPs nucleate microtubules, accelerate growth, promote or inhibit

Submitted August 29, 2019, and accepted for publication October 22, 2019.
*Correspondence: joe.howard@yale.edu
Yin-Wei Kuo and Olivier Trottier contributed equally to this work.
Editor: David Sept.
https://doi.org/10.1016/j.bpj.2019.10.027

catastrophe, increase rescue, or induce depolymerization (5,6). However, the mechanisms by which microtubule-severing enzymes regulate the microtubule cytoskeleton is not well understood.

The microtubule-severing enzymes spastin, katanin, and fidgetin are AAA-ATPases that use the chemical energy of ATP hydrolysis to sever microtubules into shorter filaments by generating internal breaks in the microtubule lattice (7–9). Microtubule severing, first observed in *Xenopus laevis* oocyte extracts (10), was initially thought of as a destructive process when the first severing enzyme katanin was discovered (7). Indeed, when katanin and spastin are overexpressed in tissue culture cells, the amount of microtubule mass is reduced (11–13). However, in vivo experiments showed, paradoxically, that genetic knockdown and mutations of severases actually reduce microtubule mass in neurons of flies and fish (14–16) and in the meiotic spindle of worms (17) and reduce the growth of longitudinal cortical microtubule arrays in plants (18). These observations suggest that severases have a nucleation-like activity.

Recent in vitro studies have demonstrated that spastin and katanin indeed possess nucleation-like activities (19,20). They promote the regrowth of severed microtubules by increasing the frequency of rescue and decreasing the shrinkage velocity and thus lead to a net increase in microtubule number and mass. An extension of the Dogterom and Leibler dynamic instability model (21) incorporating severing successfully predicted the exponential amplification of total microtubule mass observed in vitro and confirmed that the modulation of dynamics is essential to increase microtubule number and mass (19). Spastin-mediated severing also changes the length distribution of microtubules from a monotonically decreasing function to a peaked function (19). The theoretical basis of this effect, which makes the microtubules more uniformly distributed in length, is not understood.

Here, we solve an extended dynamic instability model to investigate the microtubule length distribution when the microtubule number and mass are amplified by the combination of severing and regrowth. Our work builds on earlier models of actin dynamics (22–25) in which severing is necessary to keep the mean filament length finite when the actin concentration is well above the critical concentration for growth. Severing acts as a negative feedback on length because longer filaments are cut more frequently. A similar argument holds for microtubules. However, dynamic instability (21) leads to more complex microtubule behaviors compared to actin, which does not undergo dynamic instability. A theoretical model by Tindemans and Mulder solved the case in which the microtubule number is constant (26). In this work, we solve the Tindemans and Mulder model in the case in which the microtubule number and total polymer mass increase, as is observed in vitro and in cells.

MATERIALS AND METHODS

Time evolution of microtubule lengths in the presence of severing and dynamics

In a recent study (19), we solved a generalization of the dynamic instability model (21) that includes microtubule severing (26):

$$\frac{\partial n_g}{\partial t}(x,t) = -v_g\frac{\partial n_g}{\partial x}(x,t) - f_{gs}n_g(x,t) + f_{sg}n_s(x,t) - kxn_g(x,t) + k\int_x^\infty n_g(y,t)dy \quad (1)$$

$$\frac{\partial n_s}{\partial t}(x,t) = v_s\frac{\partial n_s}{\partial x}(x,t) + f_{gs}n_g(x,t) - f_{sg}n_s(x,t) - kxn_s(x,t) + k\int_x^\infty \left[n_g(y,t) + 2n_s(y,t)\right]dy \quad (2)$$

The number of growing and shrinking microtubule plus ends of length x at time t are denoted by $n_g(x,t)$ and $n_s(x,t)$, respectively. The four dynamic parameters are represented by v_g, v_s, f_{gs}, and f_{sg}: the growth rate, shrinkage rate, catastrophe frequency, and rescue frequency, respectively. In Eqs. 1 and 2, the first three terms originate from dynamic instability. The penultimate term represents the disappearance of microtubules of length x due to severing (with severing rate k). The last term represents severing of microtubules of length greater than x into two fragments, one of which has length x.

The model makes several additional assumptions: 1) the new plus end is shrinking, whereas the new minus end is stable. This is based on the observation that around 80% of new ends satisfy this property ((18,19,27,28), but see Vemu et al., who reported a lower percentage, though this might be due to rapid rescues giving rise to apparent growing ends (20)). A nonzero probability that newly created plus ends grow can be included within the same framework and will be discussed later. 2) Microtubule dynamics is dominated by the plus ends. In other words, minus ends are considered "passive" in the sense that they neither grow nor shrink, though a minus end can disappear when the plus end depolymerizes all the way back to the minus end. This assumption is based on the reduced dynamics of minus ends, which are often capped or anchored in vivo (5,29). The model could be extended by also considering minus-end dynamics, but we have omitted this for the sake of simplicity. 3) Severing is an instantaneous event that takes place stochastically at a random location on the microtubule lattice with uniform probability. This has experimental support: the location of spastin severing events on microtubules is consistent with a uniform distribution (Fig. S1). The severing rate k is constant and has units of length^{-1}·time^{-1}. These assumptions are identical to those made by Tindemans and Mulder.

We solve the equations with the following boundary condition:

$$n_g(0^+,t) = 0 \quad (3)$$

which corresponds to the absence of stable seeds and without spontaneous nucleation. This boundary condition differs from the case solved by Tindemans and Mulder, who assumed a constant nucleation rate. In addition, unlike Tindemans and Mulder, we solve for the case in which the number of microtubules is increasing, which corresponds to the unbounded growth regime of the Dogterom and Leibler model.

Computational simulation of the stochastic severing model

To verify the existence of a length distribution at steady state, we simulated the stochastic equation for microtubule dynamics that includes severing

(Eqs. 1 and 2) together with the boundary condition (Eq. 3). The simulation starts with 100 microtubules whose lengths are sampled randomly from an exponential distribution, which is motivated by the steady-state solution of the Dogterom and Leibler dynamic instability model (21). At each time step, the length and state (growing or shrinking) of microtubules may change. In the growing state, a microtubule either grows, undergoes catastrophe and becomes a shrinking microtubule, or is severed and becomes shorter. Similarly, in the shrinking state, a microtubule either shrinks, undergoes rescue and becomes a growing microtubule, or is severed and becomes shorter. In addition, a microtubule disappears when its plus end shrinks to its minus end ($x = 0$), and each severing event creates an additional shrinking microtubule. Owing to severing and the absence of stable seeds, the total number of microtubules is not constant, and the length probability distribution is renormalized at every time point. The model's input parameters, which we refer to as the dynamic parameters, are growth rate v_g, shrinkage rate v_s, catastrophe frequency f_{gs}, rescue frequency f_{sg}, and severing rate k. The dynamic parameters in the unbounded growth regime were obtained from in vitro experiments summarized in Table 1 (19). The severing activity k is set to 0.05 $\mu m^{-1}\cdot min^{-1}$, though the value does not qualitatively affect the existence of a steady state.

Steady-state length distribution and rate of microtubule number and mass increase

When the length distribution reaches a steady state, we showed previously that the above model predicts that the total number N and mass M of microtubules increase exponentially with time:

$$N(t) = A\, e^{(k\bar{x}-v_s p_s(0^+))t} \tag{4}$$

$$M(t) = \bar{x}N(t) = A\,\bar{x}\, e^{(k\bar{x}-v_s p_s(0^+))t} \tag{5}$$

where A is a positive constant set by initial conditions, p_s is the probability density function of shrinking microtubules, and $\bar{x}$ refers to the mean length at steady state (19). The rate constant inside the exponential in Eq. 4 corresponds to the net creation of new microtubules: it is the difference between the increase in microtubules due to severing ($k\bar{x}$) and the decrease due to minus ends disappearing ($v_s p_s(0^+)$).

These equations are a consequence of the assumption that the length distribution of growing microtubules, $p_g(x, t)$, reaches a steady state and so satisfies

$$\frac{\partial p_g}{\partial t}(x,t) = \frac{\partial}{\partial t}\frac{n_g(x,t)}{N(t)} = \frac{1}{N}\frac{\partial}{\partial t}n_g(x,t) - \frac{p_g}{N}\frac{\partial N}{\partial t}(t) = 0 \tag{6}$$

Inserting Eqs. 1 and 4 into Eq. 6 gives the steady-state equation for the growing microtubule distribution:

$$\begin{aligned}(k\bar{x} - v_s p_s(0^+))p_g(x) &= -v_g\frac{\partial p_g}{\partial x}(x) - f_{gs}p_g(x) \\ &\quad + f_{sg}p_s(x) - kxp_g(x) + k\int_x^\infty p_g(y)dy\end{aligned} \tag{7}$$

Similarly, the steady-state equation for the shrinking microtubule distribution p_s is

$$\begin{aligned}(k\bar{x} - v_s p_s(0^+))p_s(x) &= v_s\frac{\partial p_s}{\partial x}(x) + f_{gs}p_g(x) - f_{sg}p_s(x) \\ &\quad - kxp_s(x) + k\int_x^\infty [p(y) + p_s(y)]dy\end{aligned} \tag{8}$$

where $p = p_g + p_s$. Summing Eqs. 7 and 8, multiplying both sides by x, and integrating from 0 to infinity,

$$(k\bar{x} - v_s p_s(0^+))\bar{x} = v_g P_g - v_s P_s \tag{9}$$

where P_g and P_s are the percentage of growing and shrinking microtubules, respectively. Using Eq. 9 and the fact that P_g and P_s sum to 1, we get

$$P_s = \frac{v_g - \bar{x}(k\bar{x} - v_s p_s(0^+))}{v_g + v_s} \tag{10}$$

$$P_g = \frac{v_s + \bar{x}(k\bar{x} - v_s p_s(0^+))}{v_g + v_s} \tag{11}$$

Integrating Eq. 7 with respect to x from 0 to infinity,

$$\left(k\bar{x} - v_s p_s(0^+) + f_{gs}\right)P_g = f_{sg}P_s \tag{12}$$

Combining Eqs. 10, 11, and 12, we obtain a characteristic equation (the same form as previously derived in (19)):

$$\begin{aligned}&\bar{x}(k\bar{x} - v_s p_s(0^+))^2 + \bar{x}\left(f_{gs} + f_{sg}\right)(k\bar{x} - v_s p_s(0^+)) \\ &\quad + v_s(k\bar{x} - v_s p_s(0^+)) - \left(f_{sg}v_g - f_{gs}v_s\right) \\ &\quad = 0\end{aligned} \tag{13}$$

which is a cubic function of the mean length $\bar{x}$ and a quadratic function of $p_s(0^+)$.

The necessary and sufficient condition to find a positive root for $k\bar{x} - v_s p_s(0^+)$, corresponding to the case in which the total mass and number of microtubule increase, is that the term $f_{sg}v_g - f_{gs}v_s$ is positive. This is the unbounded growth regime found in the Dogterom and Leibler model in which the mean length of microtubules increases indefinitely in the presence of stable microtubule seeds (21). Another way of stating this condition is that $v_g/f_{gs} > v_s/f_{sg}$: the mean length increase in the growing state is longer than the mean length decrease in the shrinking state.

TABLE 1 Summary of the Dynamic Parameters Used in the Model

Model Parameters	Input Values
Growth rate v_g	0.79 (μm/min)
Shrinkage rate v_s	9.9 (μm/min)
Catastrophe frequency f_{gs}	0.098 (min^{-1})
Rescue frequency f_{sg}	3.12 (min^{-1})
Severing rate k	0.001–0.25 ($\mu m^{-1}\cdot min^{-1}$)

The values used in the mathematical model are from previous experimental measurements (19). For testing the effect of microtubule dynamics, a severing rate of 0.05 $\mu m^{-1}\cdot min^{-1}$ was used.

Numerical integration of the steady-state differential equations

Taking derivatives with respect to x of the steady-state equations Eqs. 7 and 8 yields a system of coupled second-order ordinary differential equations (ODEs):

$$v_g p_g''(x) + \left(k\bar{x} - v_s p_s(0^+) + f_{gs} + kx\right)p_g'(x) - f_{sg}p_s'(x) + 2kp_g(x) = 0 \quad (14)$$

$$v_s p_s''(x) + f_{gs}p_g'(x) - \left(k\bar{x} - v_s p_s(0^+) + f_{sg} + kx\right)p_s'(x) - kp_g(x) - 3kp_s(x) = 0 \quad (15)$$

Evaluating Eqs. 7 and 8 at $x = 0$ gives the boundary conditions of the first derivatives:

$$p_g'(0) = \frac{f_{sg}p_s(0^+) + kP_g}{v_g} \quad (16)$$

$$p_s'(0) = \frac{-v_s p_s(0^+)^2 + \left(k\bar{x} + f_{sg}\right)p_s(0^+) - k - kP_s}{v_s} \quad (17)$$

Recall that Eq. 13 is a quadratic equation of $p_s(0^+)$ with the root

$$p_s(0^+) = \frac{2k\bar{x}^2 + a - \sqrt{a^2 + 4\bar{x}b}}{2\bar{x}v_s} \quad (18)$$

where

$$a = \bar{x}\left(f_{gs} + f_{sg}\right) + v_s \quad (19)$$

$$b = f_{sg}v_g - f_{gs}v_s \quad (20)$$

This is the only root of $p_s(0^+)$ that gives a positive value for $k\bar{x} - v_s p_s(0^+)$, which corresponds to the condition that the total mass and number increase over time with an amplification rate of

$$k\bar{x} - v_s p_s(0^+) = \frac{\sqrt{a^2 + 4\bar{x}b} - a}{2\bar{x}} \quad (21)$$

Combining these results, the boundary conditions become

$$\begin{pmatrix} p_g(0) \\ p_s(0) \\ p_g'(0) \\ p_s'(0) \end{pmatrix} = \begin{pmatrix} 0 \\ \dfrac{2k\bar{x}^2 + a - \sqrt{a^2 + 4\bar{x}b}}{2\bar{x}v_s} \\ \dfrac{f_{sg}p_s(0) + kP_g}{v_g} \\ \dfrac{\left(k\bar{x} + f_{sg} - v_s p_s(0)\right)p_s(0) - k - kP_s}{v_s} \end{pmatrix} \quad (22)$$

Using the characteristic equation, this set of boundary conditions can be expressed as a function of $\bar{x}$, the mean microtubule length, which is the only unknown parameter. The steady-state length distribution in the severing model with dynamic instability is computed numerically with MATLAB (MathWorks, Natick, MA) using *ode15s*. To integrate the solution, the boundary conditions are evaluated using an estimate for $\bar{x}$ that is iteratively fine-tuned. When the $\bar{x}$ estimate deviates from the true mean length, the solution diverges, and the divergence direction depends on whether the input $\bar{x}$ is larger or smaller than the true mean length (see example in Fig. S2 *A*; the *blue* and *red curves* diverge in opposite directions). Subsequently, a new estimate for $\bar{x}$ is calculated based on the divergence observed in the previous iteration. Specifically, the $\bar{x}$ estimate is reduced when a positive divergence was observed and vice versa. This iteration process terminates when the $\bar{x}$ estimate and the mean length calculated from the solution deviate by less than 0.001% (*scheme* in Fig. S2 *B*). The final solution converges with a pointwise accuracy of at least 10^{-5} μm^{-1}. The parameters of the numerical solution are based on the experimentally measured values (see Table 1). To explore the effect of dynamics and severing, each single parameter was altered sequentially.

As a generalization of the model, we allowed newly generated plus ends to be in the growing state with probability q. In the model above, $q = 0$. The generalizations of the master equations (Eqs. 1 and 2) are

$$\frac{\partial n_g}{\partial t}(x,t) = -v_g\frac{\partial n_g}{\partial x}(x,t) - f_{gs}n_g(x,t) + f_{sg}n_s(x,t) - kxn_g(x,t) + k\int_x^\infty \left[n_g(y,t) + qn(y,t)\right]dy \quad (23)$$

$$\frac{\partial n_s}{\partial t}(x,t) = v_s\frac{\partial n_s}{\partial x}(x,t) + f_{gs}n_g(x,t) - f_{sg}n_s(x,t) - kxn_s(x,t) + k\int_x^\infty [n_s(y,t) + (1-q)n(y,t)]dy \quad (24)$$

where $n = n_g + n_s$. The sum of Eqs. 23 and 24 is identical to the sum of Eqs. 1 and 2 and is independent of q. At the length distribution steady state, the microtubule number and mass increase exponentially with time (Eqs. 4 and 5). Following similar methods described above, we can derive the steady-state length distribution equations as

$$v_g p_g''(x) + \left(k\bar{x} - v_s p_s(0^+) + f_{gs} + kx\right)p_g'(x) - f_{sg}p_s'(x) + (2+q)kp_g(x) + kqp_s(x) = 0 \quad (25)$$

$$v_s p_s''(x) + f_{gs}p_g'(x) - \left(k\bar{x} - v_s p_s(0^+) + f_{sg} + kx\right)p_s'(x) - k(1-q)p_g(x) - k(3-q)p_s(x) = 0 \quad (26)$$

The boundary conditions for these coupled ODEs can also be derived as a function of the mean length $\bar{x}$:

$$\begin{pmatrix} p_g(0) \\ p_s(0) \\ p_g'(0) \\ p_s'(0) \end{pmatrix} = \begin{pmatrix} 0 \\ \dfrac{2k\bar{x}^2 + a - \sqrt{a^2 + 4\bar{x}b + 4k\bar{x}^2 q\left(v_g + v_s\right)}}{2\bar{x}v_s} \\ \dfrac{f_{sg}p_s(0) + kP_g + kq}{v_g} \\ \dfrac{\left(k\bar{x} + f_{sg} - v_s p_s(0)\right)p_s(0) - k(1-q) - kP_s}{v_s} \end{pmatrix} \quad (27)$$

The steady-state length distribution can then be obtained by solving Eqs. 25 and 26 numerically using the aforementioned iteration method and the boundary condition (Eq. 27).

Microtubule-severing assay

Bovine brain tubulin was purified as previously described (30). Stabilized microtubules were prepared by polymerizing unlabeled tubulin with the slowly hydrolyzable GTP analog GMP-CPP (Jena Bioscience, Jena, Germany) and affixed onto the flow channel surface with anti-tubulin antibody (clone SAP.4G5; Sigma-Aldrich, St. Louis, MO) following the previous method (31). *Drosophila* spastin was expressed and purified as previously described (19). Severing of the GMP-CPP-stabilized microtubules was performed with 3.5 nM spastin and visualized by interference reflection microscopy (32) with a frame rate of 0.5 Hz. Imaging buffer consists of 80 mM K-PIPES (pH 6.9), 1 mM $MgCl_2$, 1 mM EGTA, 50 mM KCl supplemented with 1 mM MgATP and 5 mM dithiothreitol. Analysis of the severing position was done using Fiji (33).

RESULTS AND DISCUSSION

Existence of the length distribution steady state

To verify that a steady-state length distribution exists, we performed a stochastic simulation of the microtubule-severing system (Eqs. 1 and 2, with boundary condition Eq. 3). The initial lengths of microtubules were randomly sampled from an exponential distribution with an average length of 5 μm (Fig. 1, *A* and *B*, *blue curves*). The initial proportion of shrinking microtubules was set to 10%, though we found that the system still reached the steady state regardless of this proportion. The dynamic parameters that were used in the simulation are based on previous experimental measurements (Table 1, severing rate $k = 0.05\ \mu m^{-1}\cdot min^{-1}$). The parameters lie in the unbounded growth regime, meaning that in the absence of severing, the mean microtubule length would increase indefinitely.

The microtubule length distribution converged to a steady state, which is peaked and has a decaying tail (Fig. 1 *A*). The steady-state shrinking microtubule distribution has a small fraction of zero-length microtubules, $p_s(0)$ (Fig. 1 *B*); the disappearance rate of these shrinking microtubules and the creation rate of new microtubules by severing reach a constant ratio. At steady state, the total number and mass of microtubules increased exponentially (*green solid lines* in Fig. 1, *C* and *D*), as predicted by the ODEs (Eqs. 14 and 15) and the characteristic equation (Eq. 13). Furthermore, when we increased the shrinkage rate and decreased the rescue frequency to enter the bounded growth regime, in which $f_{sg}v_g - f_{gs}v_s$ is negative, the number of microtubules went to zero (Fig. 1, *C* and *D*, *magenta dotted curves*). Thus, the stochastic model confirms the existence of a steady state and that the unbounded growth condition is an essential criterion for amplifying microtubule arrays with severing.

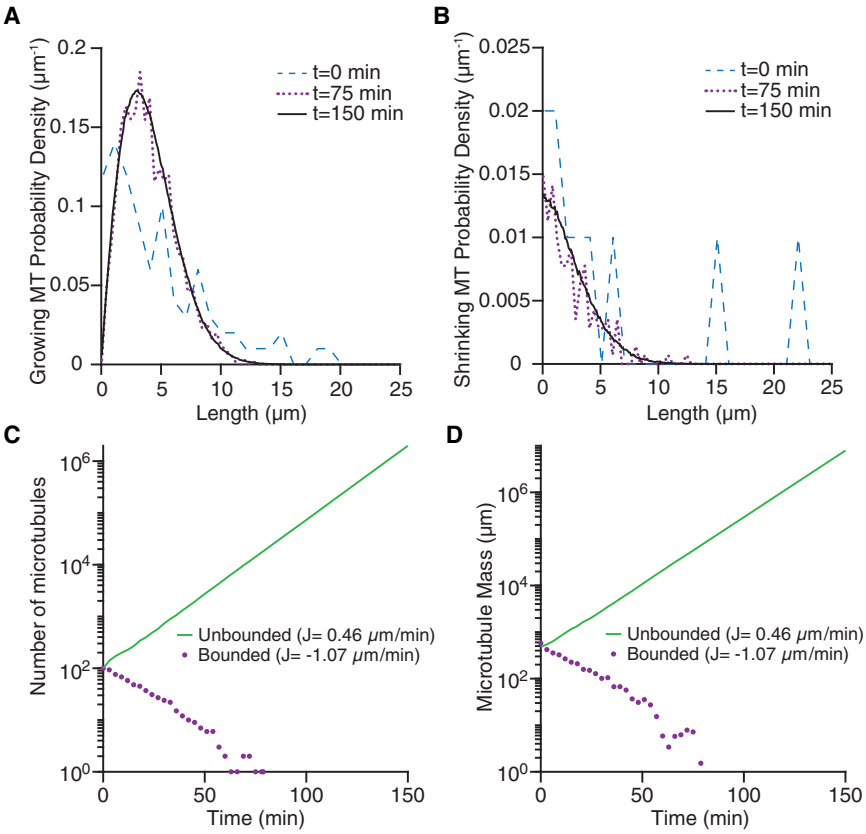

FIGURE 1 Stochastic simulation of microtubule severing. (*A* and *B*) Examples of stochastic simulations showing the temporal evolution of the length distributions of growing (*left*) and shrinking (*right*) microtubules. (*C* and *D*) The total number of microtubules (*left*) and total microtubule mass (*right*) evolving over time. In the case of unbounded growth (parameters from Table 1 with $k = 0.05\ \mu m^{-1}\cdot min^{-1}$), both the total number and the mass of microtubules increase exponentially (*green solid curve* in the semi-log plots). In the case of bounded growth (parameters from Table 1, but the shrinkage rate is increased to 20 μm/min and the rescue frequency is decreased to 1 min^{-1}), the microtubules eventually disappear (*magenta dotted curves*). The average flux of tubulin onto each microtubule, *J*, is equal to $(f_{sg}v_g - f_{gs}v_s)/(f_{sg} + f_{gs})$. To see this figure in color, go online.

Simplified no-catastrophe model

In the stochastic simulation, the total number of growing microtubules is much greater than the number of shrinking ones. This implies that, on average, microtubules spend most of their time in the growth phase. This inspired us to consider a simplified case in which the microtubules exist only in the growing state, with no catastrophe or shrinkage events. The approximate solution is valid when the effect of dynamic instability is relatively small compared to the net growth, where the tip dynamics can be approximated as a pure drift process with a small diffusion coefficient.

The time evolution of this simplified model can be expressed as

$$\frac{\partial n}{\partial t}(x,t) = -v\frac{\partial n}{\partial x}(x,t) - kxn(x,t) + 2k\int_x^\infty n(y,t)dy \quad (28)$$

where v is the microtubule elongation rate. This equation follows from Eq. 1 with $f_{sg} = 0$, $f_{gs} = 0$, $n = n_g$, $n_s = 0$, $v_g = v$, and we assume that a new plus end is in the growth phase. This equation is similar to the integro-differential equation in Edelstein-Keshet and Ermentrout (22), with the difference that the factor of 2 in the last term of Eq. 28 is replaced by 1 because only one fragment generated from severing is taken into account in their model. With the finite-length assumption, integrating Eq. 28 with respect to x from 0 to infinity and combining with the boundary condition $n(0, t) = 0$, we get

$$\frac{\partial N}{\partial t}(t) = kM(t) = k\bar{x}(t)N(t) \quad (29)$$

When the length distribution is in the steady state, the total number and mass of microtubules increase exponentially with a characteristic time $(1/k\bar{x})$. The equation for the length distribution, $p(x)$, is

$$k\bar{x}p(x) = -v\frac{\partial p}{\partial x}(x) - kxp(x) + 2k\int_x^\infty p(y)dy \quad (30)$$

Multiplying by x and integrating from 0 to infinity, we find the following expression for the mean length of the distribution:

$$\bar{x} = \sqrt{\frac{v}{k}} \quad (31)$$

Equation 30 can be solved analytically (see Appendix) by rewriting it as a Hermite differential equation, which is seen in various physical systems such as the quantum harmonic oscillator, which models the vibrations of chemical bonds (34). The final solution is

$$p(x) = \left(\frac{k}{v}\right)^{3/2}\left(x^2 + 2\sqrt{\frac{v}{k}}x\right)e^{\frac{-k\left(x^2+2\sqrt{\frac{v}{k}}x\right)}{2v}} \quad (32)$$

The solution is plotted in Fig. 2: the curve is peaked, starts at 0 when $x = 0$, and decays approximately like a Gaussian at large x. Note that the solution is dependent solely on a single parameter: the ratio of elongation rate/severing activity v/k. With increasing v/k, the distribution shifts rightwards (Fig. 2).

An important result is that the no-catastrophe model always predicts a finite mean length (provided that $k > 0$). This is explained by the fact that the severing probability increases with length. Therefore, long microtubules are quickly shortened by severing, whereas short microtubules can grow longer before they are severed. This principle also applies to the scenario with dynamic instability because the rate to sever a single microtubule will still increase with polymer length, even in the presence of shrinkage events.

Numerical solution of the dynamic instability with severing model

To understand the effect of dynamic instability on microtubule length in the presence of severing, we calculated numerically the steady-state length distributions of growing and shrinking microtubules, as well as the total microtubule population, using the ODEs Eqs. 14 and 15 (see Materials and Methods). These numerical solutions (Fig. 3, *A–C*) were in good agreement with the stochastic simulations: the simulated distributions derived from the partial differential equations (PDEs) (*open circles*) are indistinguishable from the numerical solutions of the ODEs (*solid lines*). The close agreement of the distributions implies that the mean lengths are also in agreement: the mean length of the numerical solution, 3.991 μm, is close to that of the stochastic simulation, 3.987 μm.

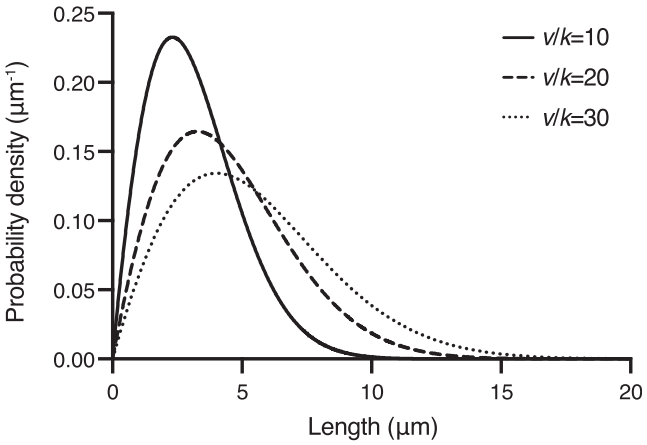

FIGURE 2 Length distribution of the no-catastrophe model. The analytic solution to the steady-state length distribution (Eq. 32) is plotted for three different values of the ratio of the growth rate/severing rate (v/k). As the ratio increases, the lengths increase, and the distribution widens.

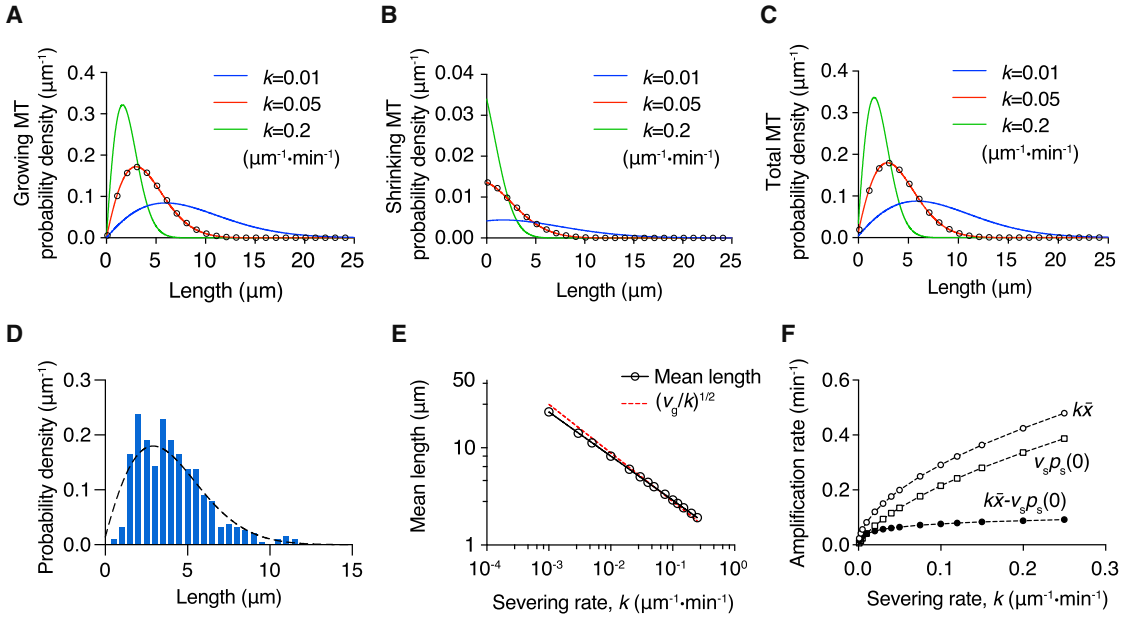

FIGURE 3 Numerical solution of the steady-state severing model with dynamic instability. Distributions of growing (*A*) and shrinking (*B*) microtubules computed numerically from the ODEs (Eqs. 14 and 15) with boundary conditions (Eq. 22) are plotted for three different severing rates k. The dynamic parameters used for the solution are contained in Table 1. More frequent cutting leads to the shortening and compaction of length distribution. (*C*) The total microtubule length distribution, which is the sum of distributions in (*A*) and (*B*). The steady-state distributions from the stochastic simulations (k = 0.05 $\mu m^{-1}\cdot min^{-1}$) are shown as open circles in (*A*)–(*C*) and agree with the ODE solutions. The proportion of shrinking microtubules is much smaller than that of growing microtubules, so the total distribution is similar to the growing one. (*D*) A comparison of the experimental length distribution (*blue histogram* (19)) with the predicted length distribution (*dashed line*, k = 0.05 $\mu m^{-1}\cdot min^{-1}$). Both distributions have a mean length of ~4 μm $\approx \sqrt{v_g/k}$. (*E*) Log-log plot of the mean length as a function of the severing rate. The open circles are the mean length obtained from the numerical solution. Black line is the linear regression of log k and log$\bar{x}$ ($R^2 > 0.9999$). Red dashed line indicates $(v/k)^{1/2}$ of the no-catastrophe model case in which $v = v_g$ = 0.79 μm/min. (*F*) Severing rate k vs. the amplification rate $k\bar{x} - v_s p_s(0^+)$ (*solid circles*), the average number of cuts on a single microtubule $k\bar{x}$ (*open circles*), and the microtubule disappearance rate $v_s p_s(0^+)$ (*squares*). These three functions all increase with severing activity, but the amplification rate quickly reaches a plateau. To see this figure in color, go online.

The total microtubule length distribution (Fig. 3 *C*) is mainly determined by the growing microtubules (Fig. 3 *A*), consistent with the stochastic simulation results, because growing microtubules are much more abundant (see Eqs. 10 and 11). The severing activity k has profound effects on both growing and shrinking microtubules: increasing severing leads to the tightening of the distribution, reduces the average length, and increases the disappearance rate $v_s p_s(0^+)$.

The model is in good agreement with the experimental results (19). With a severing rate k = 0.05 $\mu m^{-1}\cdot min^{-1}$, similar to that measured experimentally, the mean length is ~4 μm, and the predicted length distribution (*dashed line* in Fig. 3 *D*) resembles the observed one (Fig. 3 *D*, *histogram*). We have not attempted to comprehensively test the model against experiments because several of the experimental parameters are difficult to measure precisely. For example, severing can be difficult to distinguish from catastrophe, and the length distribution is difficult to measure when microtubule fragments are released from the surface. Furthermore, the theory makes simplifying assumptions such as no minus-end growth and the new plus ends always starting in the shrinking state; the experimental results show that these assumptions only hold approximately. Nevertheless, the good agreement between the measured and predicted steady-state length distributions seen in Fig. 3 *D* is a strong qualitative support for the model.

Unexpectedly, when investigating the impact of severing activity on the mean length, we found that the log-log plot is highly linear, with a slope of ~ -0.45 when the mean length (on the y axis) is plotted against the severing rate (Fig. 3 *E*, *black circles* and *line*). This power law is close to the $\bar{x} \propto k^{-1/2}$ relation in the no-catastrophe model (Eq. 31). Further comparison demonstrates that in the presence of dynamic instability, the mean length is close to the no-catastrophe case ($(v/k)^{1/2}$, Fig. 3 *E*, *red dashed line* from Eq. 31). This suggests that the addition of dynamic instability in this regime has a relatively small impact on the average length, though we do not have a good explanation for the deviation from a slope of $-1/2$.

At steady state, the total microtubule mass and number increase exponentially, and the amplification rate, $k\bar{x} - v_s p_s(0^+)$, is determined by the competition between the speed of generating new microtubules by cutting and the disappearance rate of old microtubules (Eqs. 4 and 5). With increasing severing rate, the average number of cuts

on a single microtubule $k\bar{x}$, as well as the disappearance rate $v_s p_s(0^+)$, increases (Fig. 3 *F*, *open circles* and *open squares*). The amplification rate also increases with the severing rate (Fig. 3 *F*, *solid circles*) but with a lower slope at higher severing activity. These results demonstrate that faster severing can lead to faster expansion of the microtubule network, but the effect quickly saturates with increasing cutting rate because of the shortening of lengths and higher probability of losing microtubules.

Microtubule growth rate is a key regulator of length distribution and amplification rate

Motivated by the close resemblance of the mean length in the full dynamic case and the no-catastrophe model, we next examined the effect of growth rate v_g by solving the length distribution at a severing rate $k = 0.05\ \mu m^{-1}\cdot min^{-1}$ with various growth rates, ranging from that measured with tubulin alone to that measured in high concentrations of the polymerase XMAP215 (35). Similar to the no-catastrophe case, higher growth rate leads to longer lengths of microtubules and broader length distributions (Fig. 4, *A* and *B*). Interestingly, the proportion of shrinking microtubules also increases with growth rate, whereas the disappearance probability $p_s(0^+)$ is insensitive to this change (Fig. 4 *B*). The mean length and polymerization rate also showed a power-law relation with a power of ~0.45 (Fig. 4 *C*, *black circles* and *line*). Similar to the earlier findings, the mean length can also be well-approximated by $(v_g/k)^{1/2}$ (*red dashed line* in Fig. 4 *C*). Owing to the combination of longer mean length, which increases the average number of cuts per microtubule, and the invariance of disappearance probability, the amplification rate $k\bar{x} - v_s p_s(0^+)$ shows a strong increase with the polymerization rate (Fig. 4 *D*, *solid circle*). This large increase of the amplification rate with growth rate compared to the small increase with the severing rate (Fig. 3 *F*) shows that modulation of the amplification rate is more effectively achieved by changing the growth rate rather than the severing rate, even though they both strongly affect the mean length. Thus, the polymerization rate substantially affects both the length and amplification rate of the microtubule network.

Steady-state length distribution is insensitive to other dynamic parameters

Next, we explored how the other dynamic parameters (shrinkage rate v_s, catastrophe f_{gs}, and rescue frequency f_{sg}) affect the steady-state length distribution. Constrained by the unbounded growth criterion, which is essential for increasing microtubule mass with severing, the rescue frequency has a lower bound, and the shrinkage rate and catastrophe frequency have upper bounds. We found that these parameters have a comparably small effect on the steady-state mean lengths, even when varied over physiologically relevant ranges attained in the presence of various MAPs (e.g., EB1 increases catastrophe to ~1 min^{-1} (35), CLASP increases rescues up to 10 min^{-1} (36), and spastin and TPX2 decrease shrinkage to ~5 μm/min (37)) (Fig. 5, *A–C*). In all tested conditions, the change on the mean length was within 0.5 μm (~10%).

As one might expect, a higher catastrophe frequency decreases the microtubule length (Fig. 5 *A*). However, higher rescue frequency and lower shrinkage rate actually shorten the steady-state mean length (Fig. 5, *B* and *C*), which may appear to be counterintuitive at first sight. Examining the

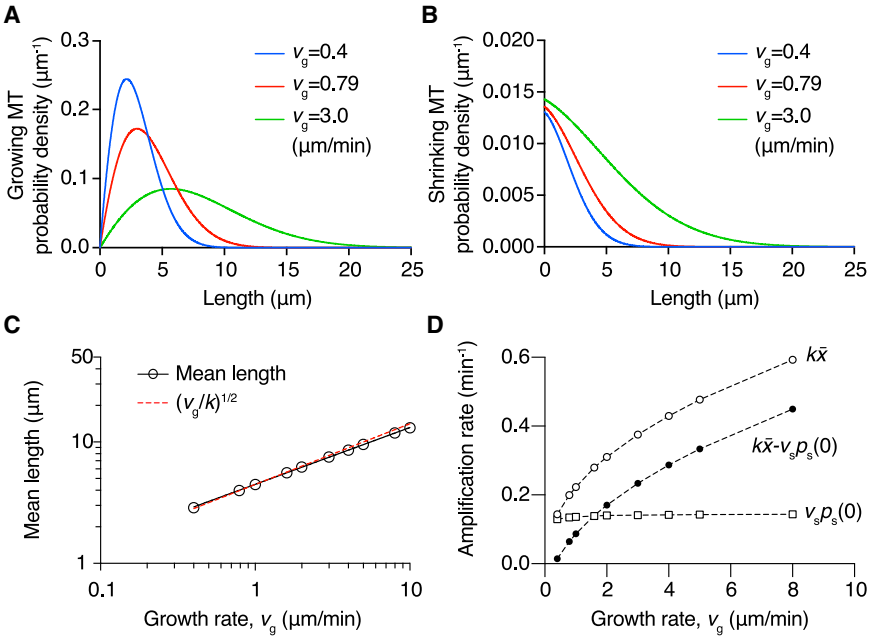

FIGURE 4 Effect of growth rate on the steady-state length distribution. The growing (*A*) and shrinking (*B*) microtubule length distributions with different growth rates v_g. The severing rate k is 0.05 $\mu m^{-1}\cdot min^{-1}$. Faster polymerization rates increase the mean length and broaden the distribution. The disappearance probability $p_s(0^+)$ varies little with the growth rate (see the *y*-intercept in *B*). (*C*) Steady-state mean length and growth rate from the numerical solution (*circles*) show a power-law relation with a slope close to 1/2 (*red dashed line*). (*D*) Amplification rate $k\bar{x} - v_s p_s(0^+)$ (*solid circles*), average number of cuts on a single microtubule $k\bar{x}$ (*open circles*), and microtubule disappearance rate $v_s p_s(0^+)$ (*squares*) vs. the growth rate v_g. The mean length increases quickly with growth rate, whereas the microtubule disappearance rate is much less affected. The amplification rate, $k\bar{x} - v_s p_s(0^+)$, therefore increases with faster growth, mainly because of the longer mean length and the increasing number of cuts on a single microtubule. To see this figure in color, go online.

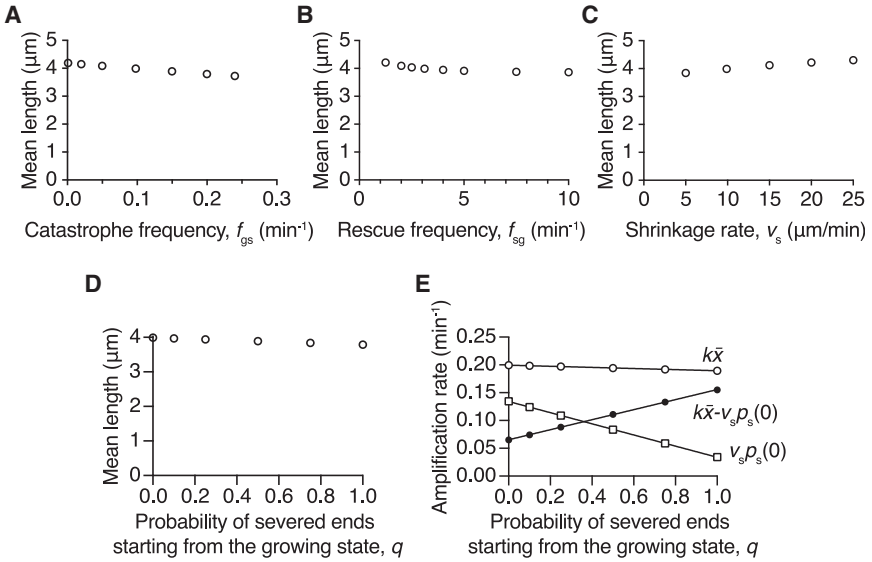

FIGURE 5 Effects of dynamic parameters on the steady-state mean length. Higher catastrophe frequency (*A*) and rescue frequency (*B*) shorten the mean length, whereas increasing the shrinkage rate leads to a longer average length (*C*). The mean length change is small. (*D*) The mean length depends only weakly on the probability that a newly generated plus end starts in the growing state, denoted by q. Earlier in this analysis we assumed that $q = 0$. (*E*) The amplification rate (*solid circles*) increases strongly with the probability that a newly generated plus end starts in the growing state. This increase is mainly due to the decrease in the rate of disappearance of microtubules (*open squares*).

length distribution in these cases revealed that this is due to the increasing survival of shorter microtubules. Lower shrinkage rate leads to an increase in shorter microtubules for both growing and shrinking states (Fig. S3, *A* and *B*). As opposed to the growth velocity, varying the shrinkage velocity has a relatively small impact on the growing microtubules (Fig. S3 *A*) but changes the shrinking microtubule distribution more prominently (Fig. S3 *B*). On the other hand, the rescue frequency modulates both the growing and shrinking microtubule distributions: a high rescue frequency increases the proportion of short growing microtubules (Fig. S3 *C*), whereas it decreases the amount of short shrinking ones (Fig. S3 *D*). Because of the dominance of growing microtubules, increasing the rescue frequency leads to an overall shorter average length (Fig. 5 *B*). Despite the mean length depending only weakly on the shrinkage rate and rescue frequency, they have a more pronounced effect on the amplification rate by modulating the microtubule disappearance rate. In conclusion, these results show that promoting rescue and slowing down shrinkage can decrease the microtubule disappearance rate and lead to a faster amplification with little effect on length.

Effect of stabilizing newly generated plus ends

All the modeling thus far has assumed that the new plus ends generated by severing start in the shrinking phase. This assumption is based on in vivo and in vitro experimental results showing that ~85% of new plus ends are shrinking (see Materials and Methods). This fraction can be regulated by plus-end binding proteins such as CLASPs (27) in cells.

To investigate how the state of the newly created plus ends affects the microtubule amount and length distribution, we extended Eqs. 1 and 2 to include the probability (denoted by q) that a newly generated end starts in the growing phase immediately after severing and obtained the new time evolution equations (Eqs. 23 and 24). The summation of these two equations is independent of q; thus, the temporal solutions of microtubule number and mass are unchanged, and both increase exponentially with time when the distribution reaches a steady state (Eqs. 4 and 5).

The steady-state length distribution can be solved numerically with the same approach (Eqs. 25, 26, and 27). Increasing the probability q is analogous to rescue promotion and leads to a slight shortening of growing microtubules (Fig. S3 *E*, the distributions shift *left* with higher q) and decreases the proportion of shrinking microtubules (Fig. S3 *F*).

The steady-state mean length is only weakly perturbed by the stabilization of the newly generated plus ends (Fig. 5 *D*) (using the dynamic parameters in Table 1). Intriguingly, the disappearance rate of microtubules ($v_s p_s(0^+)$) decreases almost linearly with q (Fig. 5 *E*, *open squares*); therefore, the stabilization of newly created plus ends (q) almost linearly increases the amplification rate (Fig. 5 *E*, *solid circles*). Thus, stabilization of severed ends can be a potent method to generate microtubules with a minor change in their length.

Comparison to a system with a steady-state number of microtubules

Previous work by Tindemans and Mulder also investigated the impact of severing on the steady-state length distribution. In their scenario, a constant spontaneous nucleation rate balances the loss of microtubules from shrinkage, leading to a constant number of microtubules (26). This corresponds to the bounded growth condition in the Dogterom and Leibler model ($f_{sg} v_g - f_{gs} v_s < 0$) (21). In contrast, we

consider the scenario in which the number of microtubules is increasing, corresponding to the unbounded growth condition ($f_{sg}v_g - f_{gs}v_s > 0$). These two scenarios give rise to important differences between the length distributions. First, in the Tindemans and Mulder scenario, the steady-state microtubule number is independent of the severing rate, whereas we show that the number increases exponentially with a rate that increases with the severing rate (Fig. 3 *F*). Second, in the Tindemans and Mulder scenario, spontaneous nucleation and the bounded growth condition together cause a high percentage of very short microtubules, whereas in our scenario, the proportion of short microtubules is small because of a higher survivability of longer microtubules (Fig. 3 *C*). Third, in the Tindemans and Mulder scenario, the ratio of the total number of growing/shrinking microtubules is equal to the ratio of the shrinkage/growth rates, whereas we found that severing introduces an additional bias toward growing microtubules (Eqs. 10 and 11) and thus gives rise to an overall increase in the total microtubule mass and number. Last, the power-law relations between the mean length and the severing or growth rate arise only in the scenario considered here (Figs. 3 *E* and 4 *C*). Thus, the constraint of constant microtubule number and the presence of spontaneous nucleation profoundly affect the length distribution and total microtubule number.

In the Tindemans and Mulder scenario, spontaneous nucleation is essential to compensate for the loss of shrinking microtubules. This scenario, which may be important in plant cells, may not be as relevant in animal cells, in which spontaneous nucleation of microtubules (away from the centrosome) is normally rare (38,39). Our results suggest that severing can also serve as a nucleation-like mechanism that rapidly increases the production of microtubules in the unbounded growth regime, regardless of the spontaneous nucleation rate. Indeed, if there is an exponential increase in new microtubules by severing and regrowth, existing nuclei or spontaneous nucleation will make decreasing contributions to the total number of new microtubules. However, if the amplification is autocatalytic, other cellular mechanisms will be required to stop this activity before free tubulin is depleted.

The similarity between models with and without dynamic instability in the presence of severing

Microtubule dynamics measurements in various systems such as sea urchin and *Xenopus* egg extracts (40,41), budding yeast (42), *Caenorhabditis elegans* (43), and tissue culture cells (44–46) have shown that the in vivo dynamic parameters are highly diverse across different species, cell lines, and cell cycle stages. Growth and shrinkage rates can span from ~0.3 to 20 μm/min and ~5–50 μm/min, respectively. Wide ranges also exist for cellular catastrophe (~0.3–10 min^{-1}) and rescue frequency (<0.1–20 min^{-1}), and subsets of highly stable microtubules with little turnover have been observed in tissue culture cells and neurons (47,48). Although our simulations have not covered this entire range, they have shown some general principles of how severing influences microtubule length and number.

A surprising finding is that the steady-state mean length can be well-approximated by the no-catastrophe simplified model (Figs. 3 *E* and 4 *C*), implying that in the presence of severing, the effect of dynamic instability on the length distribution is fairly small. This phenomenon can be understood by the fact that the total growing time of microtubules is much longer than the shrinking time and thus approximates the simplified model in which no shrinking microtubules are present.

Effect of differential severing activity on post-translational modifications and MAPs

Previous studies have revealed that the severing activities of spastin, katanin, and fidgetin depend on tubulin post-translational modifications (PTMs) and on binding of other MAPs. For example, katanin and spastin preferentially target acetylated and detyrosinated regions, which are common cellular hallmarks of stable microtubules (49,50). Fidgetin, on the other hand, has been shown to target the more labile, tyrosinated microtubules in vertebrate neurons (51,52). Microtubule stabilizers such as tau (53–56), MAP4 (57), or MAP65-1 (58) can shield microtubules from severases. PTMs and MAPs can thus bias the severing events toward a subset of microtubules in vivo.

Because the mean length in the unbounded growth condition depends on the severing rate (Fig. 3 *E*), the activities of PTM enzymes and the presence of MAPs are expected to affect the mean length. By contrast, because the rate of increase in microtubule mass is fairly insensitive to the severing rate (Fig. 3 *F*), microtubule amplification is expected to be independent of the PTM enzymes and these MAPs. Other MAPs that affect dynamic instability parameters are expected to affect microtubule length or amplification rate or both. Thus, microtubule length distributions and amplification are system properties that depend on the activities of PTM enzymes, the presence of MAPs, and on which severase is active.

CONCLUSIONS

We have used mathematical modeling to explore how microtubule dynamics affects the length distribution and the amplification rate of microtubule number and mass in the presence of severing. Unexpectedly, dynamic instability has a small impact on the steady-state length, at least over observed microtubule dynamics parameters. The microtubule length is mainly governed by the polymerization and severing rates and can be well-approximated by a simplified no-catastrophe model, which we have solved analytically. Rescue frequency, catastrophe frequency, shrinkage rate,

and the probability that newly severed ends start in the growing phase perturb the length distribution only weakly but have a more profound impact on the amplification rate. Comparison with previous experimental measurements provides strong qualitative support for our mathematical model, despite the simplifications such as omitting the minus-end dynamics and assuming severing as a single-step instantaneous process.

Cellular microtubule lengths are controlled by various machineries (59–61), including depolymerases (62–64), polymerases (65,66), the centrosome (67), severases (68), and motors (69,70). Our theoretical analysis shows that microtubule severing, in addition to shortening microtubules, also makes the microtubule length distribution more uniform. For example, the coefficient of variation of microtubule lengths (standard deviation/mean) is ~0.58 for the parameters used in Table 1 (see Fig. 3 *C*), whereas it equals 1 for the exponential distribution that solves the Dogterom and Leibler model under the bounded growth condition in the absence of severing. In this respect, severing has a similar functional consequence to the length-dependent depolymerase kinesin-8 (62), which also tightens the length distribution of dynamic microtubules (63,71). Our results also demonstrate that spastin has an effective nucleation activity: the exponential increase in microtubules is a consequence of the microtubule-dependence of severing, and in this regard, nucleation by severases is analogous to the explosive nucleation by augmin, which nucleates new microtubules from the sides of extant microtubules (61,72). Thus, our analysis provides a quantitative understanding of how severing and dynamics can jointly regulate the morphology of microtubule networks.

APPENDIX: ANALYTICAL SOLUTION OF SIMPLIFIED NO-CATASTROPHE MODEL

The master equation of the simplified no-catastrophe model reduces to the following integro-differential equation at steady state:

$$\begin{aligned} k\bar{x}p(x) &= -v\frac{\partial p}{\partial x}(x) - kxp(x) + 2k\int_x^\infty p(y)dy, \\ p(0) &= 0, \int_0^\infty p(y)dy = 1, \quad \overline{x\ \mathrm{EQ}} = \sqrt{\frac{v}{k}} \end{aligned} \tag{A1}$$

First, we differentiate with respect to x to obtain an equivalent second-order differential equation:

$$v\frac{\partial^2 p}{\partial x^2}(x) + k(x+\bar{x})\frac{\partial p}{\partial x}(x) + 3kp(x) = 0 \tag{A2}$$

Using the normalization condition on $p(x)$ (Eq. A1), we can derive a boundary condition for $(\partial p/\partial x)(0)$ that is consistent with the differential equation:

$$\frac{\partial p}{\partial x}(0) = \frac{1}{v}\left(-k\bar{x}p(0) + 2k\int_0^\infty p(y)dy\right) = \frac{2k}{v} \tag{A3}$$

Using the substitution $v = k\bar{x}^2$, the differential equation problem becomes

$$\begin{aligned} \bar{x}^2\frac{\partial^2 p}{\partial x^2}(x) + (x+\bar{x})\frac{\partial p}{\partial x}(x) + 3p(x) &= 0, \\ p(0) = 0,\ \frac{\partial p}{\partial x}(0) = \frac{2k}{v},\ \bar{x} &= \sqrt{\frac{v}{k}} \end{aligned} \tag{A4}$$

Next, we perform a change of variable to center the distribution around the mean. Let $z = (x+\bar{x})/\bar{x}$; the problem becomes

$$\begin{aligned} \frac{\partial^2 p}{\partial z^2}(z) + z\frac{\partial p}{\partial z}(z) + 3p(z) &= 0, \\ p(1) = 0,\ \frac{\partial p}{\partial z}(1) &= 2\frac{\sqrt{k}}{\sqrt{v}} \end{aligned} \tag{A5}$$

By performing the substitution $p(z) = e^{-\frac{z^2}{2}}q(z)$, the differential equation becomes

$$\begin{aligned} \frac{\partial^2 q}{\partial z^2}(z) - z\frac{\partial q}{\partial z}(z) + 2q(z) &= 0, \\ q(1) = 0,\ \frac{\partial q}{\partial z}(1) &= 2\frac{\sqrt{k}}{\sqrt{v}}e^{\frac{1}{2}} \end{aligned} \tag{A6}$$

The second-order ODE is recognized as the Hermite differential equation for the specific case in which $\lambda = 2$. The convergent solutions of the Hermite equation are known as the Hermite polynomials, which were first described by Pierre-Simon de Laplace and later by Pafnuty Chebyshev and Charles Hermite in the 1800s. Because we are seeking well-behaved solutions, we require that $q(z)$ be polynomially bounded, and the solution for $q(z)$ corresponds to the second-order Hermite polynomial

$$q(z) = C\left(z^2 - 1\right) \tag{A7}$$

where C is a constant that can be determined by the boundary condition. One notable application of Hermite polynomials in physics is the quantum harmonic oscillator, in which they give rise to the eigenstates of the Schrödinger equation (34). The solution for Eq. A6 is also found when solving the wave function of the second excited state in quantum harmonic oscillator system (vibrational quantum number $v = 2$ for a one-dimensional molecular vibrational system).

To satisfy the boundary conditions, we set $C = \left(e^{\frac{k}{v}}\right)^{1/2}$. Reverting the substitutions, the final solution becomes

$$\begin{aligned} p(x) &= \left(\frac{x^2 + 2\,x\,\bar{x}}{\bar{x}^3}\right)e^{\frac{-\left(x^2+2\,x\,\bar{x}\right)}{2\,\bar{x}^2}} \\ &= \left(\frac{k}{v}\right)^{3/2}\left(x^2 + 2\sqrt{\frac{v}{k}}x\right)e^{\frac{-k\left(x^2+2\sqrt{\frac{v}{k}}x\right)}{2\,v}} \end{aligned} \tag{A8}$$

SUPPORTING MATERIAL

Supporting Material can be found online at https://doi.org/10.1016/j.bpj.2019.10.027.

AUTHOR CONTRIBUTIONS

Y.-W.K. and J.H. formulated the model. Y.-W.K. performed the experimental measurements and numerically integrated the stochastic differential equations at steady state. O.T. solved the differential equations of the simplified model and performed the stochastic simulations. All authors wrote the manuscript.

ACKNOWLEDGMENTS

We thank the current and previous Howard lab members for their feedback on this work.

Y.-W.K. is supported by a fellowship from the Ministry of Education in Taiwan. This work was supported by National Institutes of Health Grants R01 GM110386 (to J.H.) and DP1 M110065 (to J.H.).

REFERENCES

1. Mitchison, T., and M. Kirschner. 1984. Dynamic instability of microtubule growth. *Nature*. 312:237–242.
2. Howard, J., and A. A. Hyman. 2003. Dynamics and mechanics of the microtubule plus end. *Nature*. 422:753–758.
3. Walker, R. A., E. T. O'Brien, …, E. D. Salmon. 1988. Dynamic instability of individual microtubules analyzed by video light microscopy: rate constants and transition frequencies. *J. Cell Biol.* 107:1437–1448.
4. Desai, A., and T. J. Mitchison. 1997. Microtubule polymerization dynamics. *Annu. Rev. Cell Dev. Biol.* 13:83–117.
5. Akhmanova, A., and M. O. Steinmetz. 2015. Control of microtubule organization and dynamics: two ends in the limelight. *Nat. Rev. Mol. Cell Biol.* 16:711–726.
6. Bowne-Anderson, H., A. Hibbel, and J. Howard. 2015. Regulation of microtubule growth and catastrophe: unifying theory and experiment. *Trends Cell Biol.* 25:769–779.
7. McNally, F. J., and R. D. Vale. 1993. Identification of katanin, an ATPase that severs and disassembles stable microtubules. *Cell.* 75:419–429.
8. Sharp, D. J., and J. L. Ross. 2012. Microtubule-severing enzymes at the cutting edge. *J. Cell Sci.* 125:2561–2569.
9. McNally, F. J., and A. Roll-Mecak. 2018. Microtubule-severing enzymes: from cellular functions to molecular mechanism. *J. Cell Biol.* 217:4057–4069.
10. Vale, R. D. 1991. Severing of stable microtubules by a mitotically activated protein in Xenopus egg extracts. *Cell.* 64:827–839.
11. Errico, A., A. Ballabio, and E. I. Rugarli. 2002. Spastin, the protein mutated in autosomal dominant hereditary spastic paraplegia, is involved in microtubule dynamics. *Hum. Mol. Genet.* 11:153–163.
12. McNally, K. P., O. A. Bazirgan, and F. J. McNally. 2000. Two domains of p80 katanin regulate microtubule severing and spindle pole targeting by p60 katanin. *J. Cell Sci.* 113:1623–1633.
13. Yu, W., J. M. Solowska, …, P. W. Baas. 2005. Regulation of microtubule severing by katanin subunits during neuronal development. *J. Neurosci.* 25:5573–5583.
14. Sherwood, N. T., Q. Sun, …, K. Zinn. 2004. Drosophila spastin regulates synaptic microtubule networks and is required for normal motor function. *PLoS Biol.* 2:e429.
15. Wood, J. D., J. A. Landers, …, V. T. Cunliffe. 2006. The microtubule-severing protein Spastin is essential for axon outgrowth in the zebrafish embryo. *Hum. Mol. Genet.* 15:2763–2771.
16. Stewart, A., A. Tsubouchi, …, N. T. Sherwood. 2012. Katanin p60-like1 promotes microtubule growth and terminal dendrite stability in the larval class IV sensory neurons of Drosophila. *J. Neurosci.* 32:11631–11642.
17. Srayko, M., E. T. O'toole, …, T. Müller-Reichert. 2006. Katanin disrupts the microtubule lattice and increases polymer number in *C. elegans* meiosis. *Curr. Biol.* 16:1944–1949.
18. Lindeboom, J. J., M. Nakamura, …, D. W. Ehrhardt. 2013. A mechanism for reorientation of cortical microtubule arrays driven by microtubule severing. *Science.* 342:1245533.
19. Kuo, Y. W., O. Trottier, …, J. Howard. 2019. Spastin is a dual-function enzyme that severs microtubules and promotes their regrowth to increase the number and mass of microtubules. *Proc. Natl. Acad. Sci. USA.* 116:5533–5541.
20. Vemu, A., E. Szczesna, …, A. Roll-Mecak. 2018. Severing enzymes amplify microtubule arrays through lattice GTP-tubulin incorporation. *Science.* 361:eaau1504.
21. Dogterom, M., and S. Leibler. 1993. Physical aspects of the growth and regulation of microtubule structures. *Phys. Rev. Lett.* 70:1347–1350.
22. Edelstein-Keshet, L., and G. B. Ermentrout. 2001. A model for actin-filament length distribution in a lamellipod. *J. Math. Biol.* 43:325–355.
23. Edelstein-Keshet, L., and G. B. Ermentrout. 1998. Models for the length distributions of actin filaments: I. Simple polymerization and fragmentation. *Bull. Math. Biol.* 60:449–475.
24. Ermentrout, G. B., and L. Edelstein-Keshet. 1998. Models for the length distributions of actin filaments: II. Polymerization and fragmentation by gelsolin acting together. *Bull. Math. Biol.* 60:477–503.
25. Roland, J., J. Berro, …, J. L. Martiel. 2008. Stochastic severing of actin filaments by actin depolymerizing factor/cofilin controls the emergence of a steady dynamical regime. *Biophys. J.* 94:2082–2094, Published online December 7, 2007.
26. Tindemans, S. H., and B. M. Mulder. 2010. Microtubule length distributions in the presence of protein-induced severing. *Phys. Rev. E Stat. Nonlin. Soft Matter Phys.* 81:031910.
27. Lindeboom, J. J., M. Nakamura, …, D. W. Ehrhardt. 2019. CLASP stabilization of plus ends created by severing promotes microtubule creation and reorientation. *J. Cell Biol.* 218:190–205, Published online October 30, 2018.
28. Zhang, Q., E. Fishel, …, R. Dixit. 2013. Microtubule severing at crossover sites by katanin generates ordered cortical microtubule arrays in Arabidopsis. *Curr. Biol.* 23:2191–2195.
29. Dammermann, A., A. Desai, and K. Oegema. 2003. The minus end in sight. *Curr. Biol.* 13:R614–R624.
30. Castoldi, M., and A. V. Popov. 2003. Purification of brain tubulin through two cycles of polymerization-depolymerization in a high-molarity buffer. *Protein Expr. Purif.* 32:83–88.
31. Gell, C., V. Bormuth, …, J. Howard. 2010. Microtubule dynamics reconstituted in vitro and imaged by single-molecule fluorescence microscopy. *Methods Cell Biol.* 95:221–245.
32. Mahamdeh, M., S. Simmert, …, J. Howard. 2018. Label-free high-speed wide-field imaging of single microtubules using interference reflection microscopy. *J. Microsc.* 272:60–66.
33. Schindelin, J., I. Arganda-Carreras, …, A. Cardona. 2012. Fiji: an open-source platform for biological-image analysis. *Nat. Methods.* 9:676–682.
34. Atkins, P. W., J. de Paula, and J. Keeler. 2018. Atkins' Physical Chemistry: Molecular Thermodynamics and Kinetics. Oxford University Press, Oxford.
35. Zanic, M., P. O. Widlund, …, J. Howard. 2013. Synergy between XMAP215 and EB1 increases microtubule growth rates to physiological levels. *Nat. Cell Biol.* 15:688–693.
36. Lawrence, E. J., G. Arpag, …, M. Zanic. 2018. Human CLASP2 specifically regulates microtubule catastrophe and rescue. *Mol. Biol. Cell.* 29:1168–1177.
37. Reid, T. A., B. M. Schuster, …, M. K. Gardner. 2016. Suppression of microtubule assembly kinetics by the mitotic protein TPX2. *J. Cell Sci.* 129:1319–1328.
38. Wieczorek, M., S. Bechstedt, …, G. J. Brouhard. 2015. Microtubule-associated proteins control the kinetics of microtubule nucleation. *Nat. Cell Biol.* 17:907–916.

39. Petry, S., and R. D. Vale. 2015. Microtubule nucleation at the centrosome and beyond. *Nat. Cell Biol.* 17:1089–1093.

40. Gliksman, N. R., S. F. Parsons, and E. D. Salmon. 1992. Okadaic acid induces interphase to mitotic-like microtubule dynamic instability by inactivating rescue. *J. Cell Biol.* 119:1271–1276.

41. Belmont, L. D., A. A. Hyman, …, T. J. Mitchison. 1990. Real-time visualization of cell cycle-dependent changes in microtubule dynamics in cytoplasmic extracts. *Cell.* 62:579–589.

42. Shaw, S. L., E. Yeh, …, K. Bloom. 1997. Astral microtubule dynamics in yeast: a microtubule-based searching mechanism for spindle orientation and nuclear migration into the bud. *J. Cell Biol.* 139:985–994.

43. Lacroix, B., K. G. Bourdages, …, A. S. Maddox. 2014. In situ imaging in *C. elegans* reveals developmental regulation of microtubule dynamics. *Dev. Cell.* 29:203–216.

44. Sammak, P. J., and G. G. Borisy. 1988. Direct observation of microtubule dynamics in living cells. *Nature.* 332:724–726.

45. Shelden, E., and P. Wadsworth. 1993. Observation and quantification of individual microtubule behavior in vivo: microtubule dynamics are cell-type specific. *J. Cell Biol.* 120:935–945.

46. Salaycik, K. J., C. J. Fagerstrom, …, P. Wadsworth. 2005. Quantification of microtubule nucleation, growth and dynamics in wound-edge cells. *J. Cell Sci.* 118:4113–4122.

47. Schulze, E., and M. Kirschner. 1987. Dynamic and stable populations of microtubules in cells. *J. Cell Biol.* 104:277–288.

48. Kapitein, L. C., and C. C. Hoogenraad. 2015. Building the neuronal microtubule cytoskeleton. *Neuron.* 87:492–506.

49. Sudo, H., and P. W. Baas. 2010. Acetylation of microtubules influences their sensitivity to severing by katanin in neurons and fibroblasts. *J. Neurosci.* 30:7215–7226.

50. Riano, E., M. Martignoni, …, E. I. Rugarli. 2009. Pleiotropic effects of spastin on neurite growth depending on expression levels. *J. Neurochem.* 108:1277–1288.

51. Leo, L., W. Yu, …, P. W. Baas. 2015. Vertebrate fidgetin restrains axonal growth by severing labile domains of microtubules. *Cell Reports.* 12:1723–1730.

52. Hu, Z., J. Feng, …, M. Liu. 2017. Fidgetin regulates cultured astrocyte migration by severing tyrosinated microtubules at the leading edge. *Mol. Biol. Cell.* 28:545–553.

53. Qiang, L., W. Yu, …, P. W. Baas. 2006. Tau protects microtubules in the axon from severing by katanin. *J. Neurosci.* 26:3120–3129.

54. Qiang, L., W. Yu, …, P. W. Baas. 2010. Basic fibroblast growth factor elicits formation of interstitial axonal branches via enhanced severing of microtubules. *Mol. Biol. Cell.* 21:334–344.

55. Siahaan, V., J. Krattenmacher, …, M. Braun. 2019. Kinetically distinct phases of tau on microtubules regulate kinesin motors and severing enzymes. *Nat. Cell Biol.* 21:1086–1092.

56. Tan, R., A. J. Lam, …, R. J. McKenney. 2019. Microtubules gate tau condensation to spatially regulate microtubule functions. *Nat. Cell Biol.* 21:1078–1085.

57. McNally, K. P., D. Buster, and F. J. McNally. 2002. Katanin-mediated microtubule severing can be regulated by multiple mechanisms. *Cell Motil. Cytoskeleton.* 53:337–349.

58. Burkart, G. M., and R. Dixit. 2019. Microtubule bundling by MAP65-1 protects against severing by inhibiting the binding of katanin. *Mol. Biol. Cell.* 30:1587–1597.

59. Mohapatra, L., B. L. Goode, …, J. Kondev. 2016. Design principles of length control of cytoskeletal structures. *Annu. Rev. Biophys.* 45:85–116.

60. Goshima, G., R. Wollman, …, R. D. Vale. 2005. Length control of the metaphase spindle. *Curr. Biol.* 15:1979–1988.

61. Decker, F., D. Oriola, …, J. Brugués. 2018. Autocatalytic microtubule nucleation determines the size and mass of *Xenopus laevis* egg extract spindles. *eLife.* 7:e31149.

62. Varga, V., J. Helenius, …, J. Howard. 2006. Yeast kinesin-8 depolymerizes microtubules in a length-dependent manner. *Nat. Cell Biol.* 8:957–962.

63. Gardner, M. K., M. Zanic, …, J. Howard. 2011. Depolymerizing kinesins Kip3 and MCAK shape cellular microtubule architecture by differential control of catastrophe. *Cell.* 147:1092–1103.

64. Varga, V., C. Leduc, …, J. Howard. 2009. Kinesin-8 motors act cooperatively to mediate length-dependent microtubule depolymerization. *Cell.* 138:1174–1183.

65. Reber, S. B., J. Baumgart, …, F. Jülicher. 2013. XMAP215 activity sets spindle length by controlling the total mass of spindle microtubules. *Nat. Cell Biol.* 15:1116–1122.

66. Hibbel, A., A. Bogdanova, …, J. Howard. 2015. Kinesin Kip2 enhances microtubule growth in vitro through length-dependent feedback on polymerization and catastrophe. *eLife.* 4:10542.

67. Greenan, G., C. P. Brangwynne, …, A. A. Hyman. 2010. Centrosome size sets mitotic spindle length in *Caenorhabditis elegans* embryos. *Curr. Biol.* 20:353–358.

68. Loughlin, R., J. D. Wilbur, …, R. Heald. 2011. Katanin contributes to interspecies spindle length scaling in Xenopus. *Cell.* 147:1397–1407.

69. Marshall, W. F., and J. L. Rosenbaum. 2001. Intraflagellar transport balances continuous turnover of outer doublet microtubules: implications for flagellar length control. *J. Cell Biol.* 155:405–414.

70. Hepperla, A. J., P. T. Willey, …, M. K. Gardner. 2014. Minus-end-directed kinesin-14 motors align antiparallel microtubules to control metaphase spindle length. *Dev. Cell.* 31:61–72.

71. Gardner, M. K., M. Zanic, and J. Howard. 2013. Microtubule catastrophe and rescue. *Curr. Opin. Cell Biol.* 25:14–22.

72. Petry, S., A. C. Groen, …, R. D. Vale. 2013. Branching microtubule nucleation in Xenopus egg extracts mediated by augmin and TPX2. *Cell.* 152:768–777.